Nanoscale

PAPER

View Article Online
View Journal | View Issue

Check for updates

Cite this: *Nanoscale*, 2025, **17**, 18202

Field-induced demagnetisation of bisegmented cylindrical ferromagnetic nanowires mediated by skyrmion tubes†

João Fradet, *[a] Victor Vega, [b] Yolanda Álvarez, [c] Javier García, [c] Cristina Bran, [d] Victor M. Prida, [c] Agustina Asenjo [a] and Oksana Chubykalo-Fesenko [a]

Received 11th April 2025,
Accepted 5th July 2025

DOI: 10.1039/d5nr01471a

rsc.li/nanoscale

Cylindrical magnetic nanowires offer exciting possibilities for potential applications in spintronic devices that rely on manipulation of topologically non-trivial three-dimensional domain walls. This work investigates field-induced magnetisation processes in bisegmented FeCo nanowires, with sharp diameter modulation, specially designed for the controlled nucleation of magnetic domain walls. By employing variable-field magnetic force microscopy techniques and micromagnetic simulations, we observe that domain wall nucleation, specifically of the Bloch-point type, is mediated by an intermediate skyrmion tube texture that closes the stray field lines, making it detectable by a magnetic force microscopy probe. The simulations further demonstrate that domain wall motion is chirality-dependent; domain walls with non-aligned chirality relative to the direction of spin precession are halted by the emission of surface spin waves, which also switch the domain wall chirality. In the case of aligned chirality, domain walls propagate freely. These findings provide novel insight into the nucleation, stabilization, and motion of complex domain wall textures in cylindrical nanowires and contribute to the understanding of curvature-dependent magnetic phenomena, with implications for designing high-speed domain wall-based devices.

Introduction

The development of nanofabrication methods, in particular the growth of self-organised nanoporous structures by anodisation of aluminum,[1,2] has led to increased scientific interest in cylindrical magnetic nanowires (NWs), as these porous membranes could be used as patterned templates for electrodeposition.[3] This interest is accompanied by the emergence of new fields with promising technological applications such as 3D magnetism[4] as well as more fundamental research on the influence of curvature on magnetism.[5]

In ferromagnetic NWs, the curvature of the cylindrical geometry stabilises a number of complex 3D magnetic textures such as vortex–antivortex domain walls (VAV-DWs) and Bloch-point domain walls (BP-DWs). In the latter case, the magnetisation curls azimuthally around a point singularity where the magnetisation vanishes.[6,7] The dynamics of these DWs were predicted to suppress the Walker breakdown that hinders DW propagation in nanostripes due to the symmetry of dipolar fields in cylindrical geometry, and the velocity would only be limited as it reaches the magnon group velocity, emitting spin waves due to the spin-Cherenkov effect.[8] However, topological transformations have been observed even in cylindrical geometry, possibly hindering the DW velocity.[9] Although these dynamic transformations are typically associated with a Walker breakdown effect, hampering its mobility, in high magnetisation NWs like iron-based NWs, such transformations can actually accelerate the DW motion beyond the magnonic limit, reaching velocities up to 14 km s^{-1}.[10] The study of DW dynamics in cylindrical NWs is therefore paramount for the development of DW-based spintronic devices.

Micromagnetic modelling also showed that the dynamics of demagnetisation processes in cylindrical nanowires can be mediated by the formation of core–shell textures such as vortex and skyrmion tube-like structures.[11,12] The signatures of these complex magnetisation reversal mechanisms have been intuited experimentally in multi-segmented diameter-modulated NWs.[13,14] Importantly, the predictions show that demagnetisation processes *via* skyrmion tubes take place in cylindrical NWs with large differences in diameters between seg-

---

[a] *Instituto de Ciencia de Materiales de Madrid, CSIC, 28049 Madrid, Spain. E-mail: joao.fradet@csic.es*
[b] *Laboratorio Membranas Nanoporosas, SCTs Edificio Severo Ochoa, Universidad de Oviedo, 33006-Oviedo, Spain*
[c] *Departamento de Física, Facultad de Ciencias, Universidad de Oviedo, 33007-Oviedo, Spain*
[d] *Instituto de Nanociencia y Materiales de Aragón, CSIC, Zaragoza, Spain*

† Electronic supplementary information (ESI) available. See DOI: **https://doi.org/10.1039/d5nr01471a**

ments,[12] a geometry that is not easily experimentally accessible by the nanofabrication process through voltage-controlled hard anodisation (HA) of aluminum.[15] Although the DW motion in cylindrical NWs has been widely studied, not much attention has been paid to their nucleation processes, particularly in experiments. Since DWs are typically nucleated at the NW ends, one can engineer each NW segment's shape anisotropy such that the DW is nucleated at a particular end. Indeed, the DW nucleation field of cylindrical nanowires decreases as the diameter increases.[16] One possibility is to produce the ferromagnetic segments of increasing lengths separated by thin non-magnetic segments to achieve a ratchet-like behaviour of magnetisation reversal initiated in the shortest ferromagnetic segment.[17] This method is not adequate for the study of DWs since it requires interruptions of ferromagnetism along the NW, which result in the DWs being sequentially nucleated and annihilated at the non-magnetic segments and the process is mediated by a combination of the externally applied field and the stray field from the reversed segment, with increasing energy requirement. Additionally, geometric asymmetries can enable chirality control; for instance, it has been shown that interface tilting in multilayered cylindrical nanowires allows for controlled manipulation of chirality.[18]

Another possibility is to use a bisegmented NW (BNW) with magnetically soft and hard materials such as nickel and cobalt.[19–21] In this case, a domain wall nucleates at the end of the segment of the material, which is magnetically softer, and the DW pins at the interface between the two materials.[22] In this study, we explore an alternative approach facilitated by recently developed nanofabrication techniques that combine atomic layer deposition (ALD)[23] with conventional hard anodisation of aluminum,[15] enabling the fabrication of BNWs with significant diameter modulation.[24–26] A DW then should require less energy to nucleate at the wide segment end of the BNW rather than at the thin one. We take a close look at the magnetisation reversal process of bisegmented FeCo nanowires with a large diameter difference by micromagnetic simulations and variable-field magnetic force microscopy (VF-MFM). Our results provide further insight into the possibility of fully controlling the DW nucleation and propagation in cylindrical geometries.

Results

A schematic of the studied bisegmented nanowire is shown in Fig. 1. The ratio between the wide and narrow segments d/D is about 1/3 and the material in question is a ferromagnetic FeCo alloy with large saturation magnetisation.

To gain insight into the nature of demagnetisation processes under an applied magnetic field in our bisegmented $\mathrm{Fe}_{65}\mathrm{Co}_{35}$ nanowires, we first present the theoretical analysis of the expected behavior. This is done by micromagnetic simulations (see the Methods section). In soft magnetic nanowires, shape anisotropy dominates over the magnetocrystalline one, and the magnetisation at the remanence is expected to be longitudinal with respect to the BNW long axis, with curling of the magnetisation at both the BNWs' ends and at the diameter modulation, in order to reduce the magnetic surface charges.[27] Due to the local stray field, a DW should nucleate at the wide end of the BNW and then propagate, reversing the magnetisation. The rotational sense of magnetisation curling in these structures at the BNW ends (vorticity) may be arbitrary or defined by local inhomogeneities or magnetic history. We consider the two cases corresponding to different rotational senses of these spin textures at the wide end of the BNW where magnetisation reversal is expected to initiate.

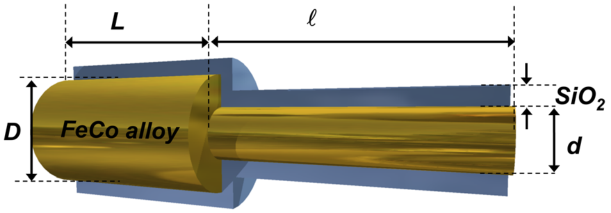

Fig. 1 Schematic diagram of diameter-modulated FeCo BNWs, indicating their main morphological parameters: D, d, L, and l (diameters and lengths of the wide and narrow segments, respectively).

We define chirality as a product of the DW propagation direction (positive or negative) and vorticity. In the first case, as shown in Fig. 2, the sense of rotation of the curling structure matches the applied field direction following the right-hand rule, named in ref. 8 as the "good" chirality. Conversely, when the vorticity is opposite to that set by the applied field, it is named the "bad" chirality and is shown in Fig. 3. The figures show sets of three images during the magnetisation reversal of bisegmented FeCo nanowires. Each set corresponds to magnetisation states at different applied fields or at a different time after the field is increased. These dynamic states are important, as they are often pinned at defects along the BNW. In each set, the bottom image shows the Z component of magnetisation at the NWs' surface giving information on the vorticities of the magnetic textures. The middle image shows the X component of the magnetisation at the surface (in the transparent image) and the $X = 0$ isosurface in green, delineating the DW profile and the skyrmion tube textures inside the BNW. The green sphere represents the BP position where the three components of magnetisation vanish. Lastly, the top image shows a phase map for an MFM image calculated from each magnetisation state (see the Methods section). When necessary, cross-sections along the BNW are shown in the insets.

Starting from remanence, the external field is ramped up to 18 mT, just before the switching field. The curling structure at the wide end of the NW expands into a vortex tube texture where the surface spins rotate around the core, still pointing antiparallel to the magnetic field. Simultaneously, the surface spins slightly rotate parallel to the applied magnetic field, as evidenced by the appearance of the isosurface $X = 0$. This leads to a compensation of the magnetic charges as the magnetic flux lines close, resulting in a loss of contrast of the predicted

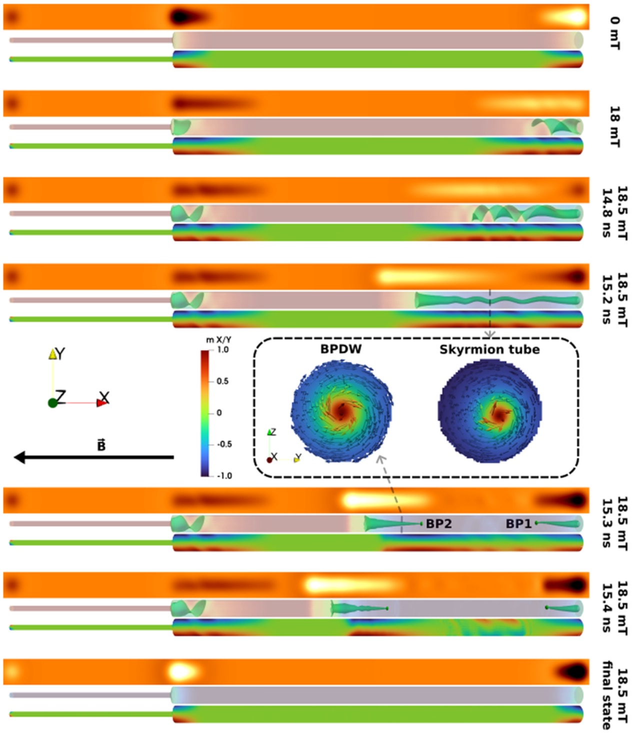

Fig. 2 Sets of three images for different stages of magnetisation reversal for the DW nucleated at the wide BNW end with "good" chirality. The top image plots the calculated MFM image using simulation data. The middle image shows the X component of magnetisation in a transparent BNW surface showing the isosurface $X = 0$ in green and the green spheres represent a Bloch point defined as the intersection of the isosurfaces $X = 0$, $Y = 0$ and $Z = 0$. The bottom image plots the Z component of magnetisation at the BNW surface. The inset shows X cross-sections of the BNW when deemed necessary. The colour bar represents the X component of magnetisation in the middle images and the insets and the Z component of magnetisation in the bottom images.

MFM image, as seen at 18 mT in Fig. 2 and 3, respectively. In both cases, at 18.5 mT, the magnetisation reverses in a single step by a DW nucleation–propagation process. Although DW nucleation in the good chirality case takes a longer time, in both cases there are qualitative similarities in the overall process, especially if only final states and not the dynamics are considered. The vortex tube configuration keeps expanding as the surface spins further rotate anti-parallel to the core. At this point, the negative magnetic charges at the wide end overcome the positive ones, resulting in the appearance of a slight dark spot in the MFM image, as seen at times 14.7 ns and 2.3 ns in Fig. 2 and 3, respectively.

It is noteworthy that when the magnetic field is applied (18 mT), a second vortex tube simultaneously forms at the diameter modulation, as evidenced by the isosurface in the set of images "0 ns" in Fig. 2 and 3. Eventually, at 15.1 ns after the field reaches 18.5 mT for "good" chirality (Fig. 2) and at 2.6 ns after applying 18 mT for "bad" chirality (Fig. 3), the surface spins align close to the field direction in all azimuthal directions, antiparallel to the core and forming a skyrmion tube texture.

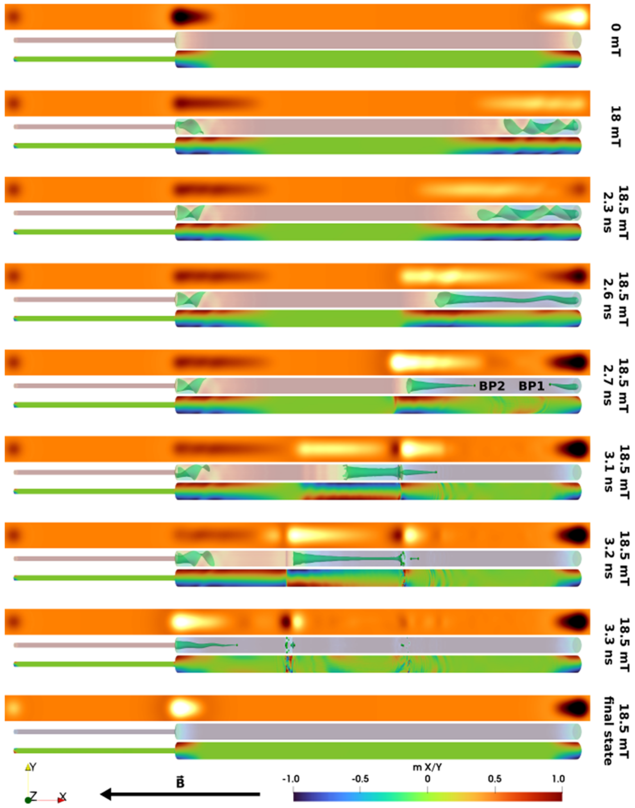

Fig. 3 Sets of three images for different stages of magnetisation reversal for the DW nucleated at the wide BNW end with a "bad" chirality. The top image plots the calculated MFM image using simulation data. The middle image shows the X component of magnetisation in a transparent NW surface showing the isosurface $X = 0$ in green and the green spheres represent a Bloch point defined as the intersection of the isosurfaces $X = 0$, $Y = 0$ and $Z = 0$. The bottom image plots the Z component of magnetisation at the BNW surface. The inset shows X cross-sections of the NW when deemed necessary. The colour bar represents the X component of magnetisation in the middle images and the insets and the Z component of magnetisation in the bottom images.

As the demagnetisation/remagnetisation stage further proceeds, the core shrinks and the skyrmion tube reaches a critical length above which it is no longer stable. At this point, at 15.1 ns for the "good" chirality case shown in Fig. 2 and at 2.7 ns for the "bad" chirality case, the core of the skyrmion tube breaks with the injection of a pair of Bloch points, resulting in the nucleation of two BP-DWs. One of the BPs (BP1) is ejected through the NWs' wide end, and the propagation of the DW containing BP2 initiates the switching of magnetisation.

Due to a reduced magnetostatic field at the surface, the spins on the DW have a lower mobility at the BNW surface, resulting in a cone-shaped DW, as shown in Fig. 1 and 2, with the BP lagging behind the surface spins. This is in agreement with earlier predictions for BP-DW motion.[10,27,28] However, the DW dynamics differ significantly for the "good" and "bad" chirality cases. Whilst in the former case, the DW moves linearly with no transformations, in the latter case, the vorticity of the DW does not match the natural precessional direction of the spins, which leads to instabilities in the DW motion that switch the chirality of the DW.

From the 6th set of images in Fig. 3, at 3.1 ns after the switching field was applied, we see that immediately after nucleation, the DW emits chiral spin waves in the propagation direction, which halts the DW motion. These chiral spin waves effectively curl the magnetisation opposite to the DW chirality, resulting in the formation of a second skyrmion tube separated from the BP by a complex clockwise–anticlockwise texture. Further propagation is then achieved by breaking the skyrmion tube through an integrated pair creation and annihilation process, as seen at 3.2 ns. The remaining BP will then be of the "good" chirality type, completing the chirality switch and the DW will then propagate without further transformation or instabilities. This chirality switching process is similar to that previously described for ferromagnetic nanotubes[29] and also for current-driven DWs in nanowires.[30] Therefore, independently of the chirality of the initially nucleated DW, it will always be of "good" chirality as it approaches the diameter modulation. This again results in two distinct possibilities, also related to the matching of vorticities.

As shown in Fig. 2, the vorticity of the vortex at the modulation matches the approaching "good" chirality DW. Conversely, as shown in Fig. 3, the vorticity is opposite to the now "good" chirality approaching the DW. In the first case, when the vorticities match, the vortex will seamlessly merge into a conical shaped DW and the BP will penetrate into the narrow segment. In the opposite case in Fig. 3, the vortex at the modulation repels the DW as the vorticities are antiparallel to each other. This again forms a clockwise–anticlockwise texture, similar to the one seen during the BP-DW chirality switching process, which is annihilated by the injection of pairs of BPs at 3.3 ns, as shown in Fig. 3, and the DW will have the "bad" chirality as it enters the narrow segment. It is noteworthy that in the narrow segment, the instabilities associated with the field-induced "bad" chirality DW motion merely affect the DW mobility and do not induce a chirality switch. This may be attributed to the fact that in the smaller diameter segment, the surface spins do not have enough space to curl enough to induce a chirality switch.

In the ESI,† the results for the nickel BNW are shown, revealing a qualitatively similar magnetisation reversal process.

Experimentally, bisegmented nanowires with a sharp diameter modulation were prepared by electrodeposition into hard anodic nanoporous alumina templates (see the Methods section). The morphological characterization of diameter-modulated FeCo BNWs is summarized in Fig. 4. The sharp modulation of the pore diameter achieved through the combination of hard anodization (HA) and atomic layer deposition (ALD) coatings can be observed in the cross-sectional SEM image of the empty HA membrane, as shown in Fig. 4(a). Fig. 4(b) evidences that the electrochemically deposited FeCo alloy nanowires successfully reproduce this morphological feature. The sharp diameter modulation becomes even more evident in the TEM image, as shown in Fig. 4(c), in which the diameters of the narrow and wide segments of the nanowire can be accurately measured.

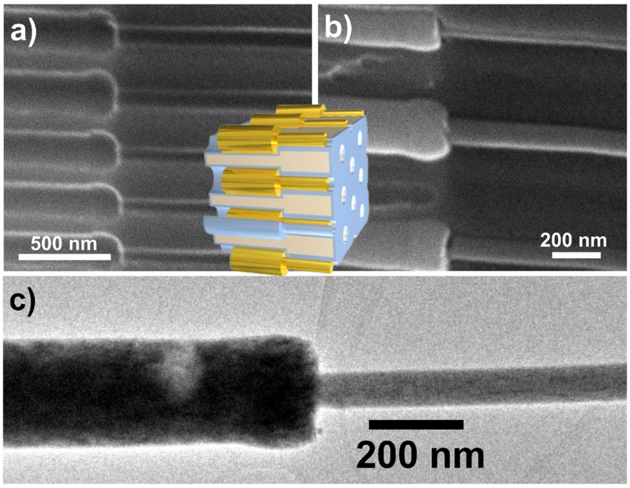

Fig. 4 (a) SEM image of pore diameter modulation in the cross-section of an empty HA nanoporous alumina membrane. (b) SEM image of diameter-modulated FeCo bisegmented nanowires, embedded into the pores of an HA alumina membrane. (c) HR-TEM image of a diameter-modulated FeCo BNW. The inset in (a and b) shows a schematic view of the diameter-modulated nanowires embedded into the HA template.

From the morphological characterization, we can conclude that the experimental sample design is that shown in the schematic diagram in Fig. 1, with the lengths of the narrow and wide segments of l = 10 μm and L = 12 μm, whilst their diameter values are d = 90 and D = 250 nm, respectively. The composition of the FeCo alloy, as measured by EDX analysis carried out in both SEM and TEM characterization studies (not shown here), is approximately $Fe_{65}Co_{35}$.

Individual nanowires were released from the template and magnetisation processes under an applied field were studied

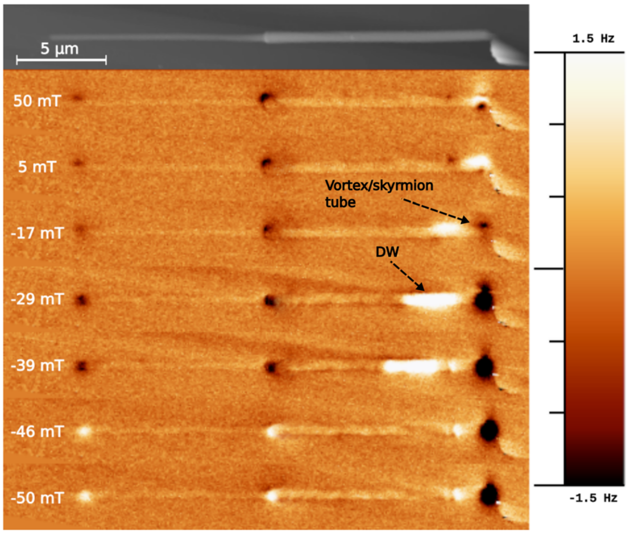

Fig. 5 MFM images at different externally applied fields obtained in sequence. The top image is a topographic map of the BNW. The MFM signal is measured as a change in the cantilevers' oscillation frequency.

by magnetic force microscopy (MFM). MFM images lack chirality information, and experimentally determining chirality in cylindrical nanowires remains challenging. Only quantitative techniques like electron holography, XMCD-PEEM, and scanning nitrogen-vacancy magnetometry[7,31] offer direct insights into their chiral magnetic structure. However, variable field MFM provides valuable insights into the magnetization reversal process. Fig. 5 shows a series of MFM images at different applied magnetic fields, taken in sequence from near saturation at 50 mT down to −50 mT with a completely reversed magnetisation. As expected, due to the difference in local shape anisotropies, the reversal process starts at the end of the wide segment by the nucleation and subsequent propagation of a DW. In the first two images, taken at positive fields, the magnetisation remains close to saturation, whereas in the last two images, the magnetisation is fully reversed. After remanence, at −17 mT, the bright spot at the wide end moves inward, leaving a slightly dark spot in its place.

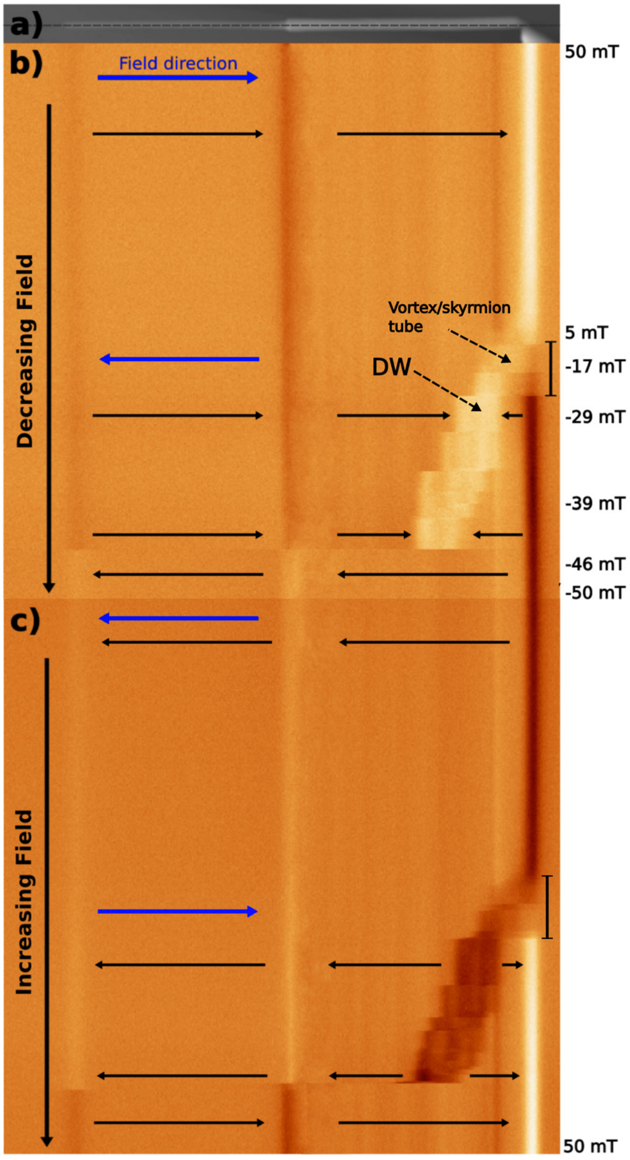

Fig. 6 3D-mode imaging of the FeCo BNW, plotted against an external field applied parallel to the NWs' long axis. (a) Standard AFM topography map. The grey dashed line represents the line, which is repeatedly scanned for the 3D mode measurement. (b and c) 3D plots for decreasing and increasing magnetic fields, respectively. The black horizontal arrows represent the magnetisation direction. The bracket around −17 mT indicates the magnetic configurations for which the magnetic charges are compensated at the right end of the BNW.

The magnetic behaviour of the MFM signal is in agreement with the DW nucleation process described above and corresponds to the expansion of the vortex tube into the BNW seen at 14.7 and 2.3 ns after −18.5 mT was applied, as shown in Fig. 2 and 3, respectively. Indeed, the blue colour in the simulation images already indicates a slight alignment of surface spins anti-parallel to the core closing the stray field lines.

At −29 and −39 mT, the dark-bright-dark contrast sequence is indicative of a DW pinned at slightly different positions. One should note that, in contrast to the dynamic states computed by micromagnetic simulations, these are equilibrium configurations imaged at particular applied magnetic fields. In the simulations, similar situations correspond to intermediate dynamic stages and in the experiment we believe that the presence of defects provides pinning sites, making some of the dynamic states temporarily stable.

A more complete picture of the magnetisation reversal process is provided by the 3D mode measurement (Fig. 6), where the same line over the BNW (Fig. 6(a)) is scanned under a changing magnetic field. The magnetic field starts at 50 mT and decreases down to −50 mT, as shown in Fig. 6(b), whereupon it increases back again up to 50 mT, as shown in Fig. 6(c), imaging the hysteresis loop of magnetisation. The magnetisation remains close to saturation until just after remanence, at which point the bright spot contrast at the wide end diminishes and the white-contrast region further expands into the BNW. Simultaneously, the magnetic charges at the wide end reduce. The spot at the wide end then darkens as the surface spins align antiparallel to the core closing the flux lines, eventually forming a skyrmion-like tube texture as represented in the fourth set of images (images 15.1 and 2.6 ns,

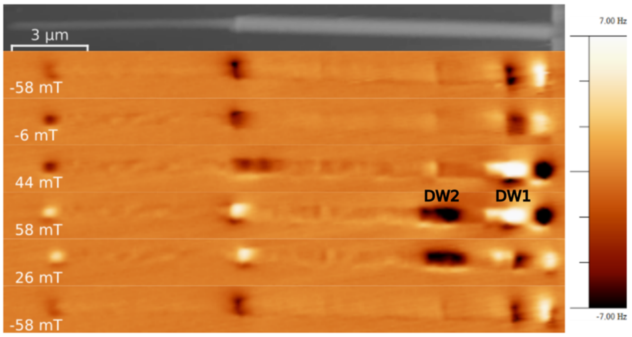

Fig. 7 MFM images at different externally applied fields measured in sequence. The top image is a topographic map of the BNW. The MFM signal is measured as a change in the cantilevers' oscillation frequency.

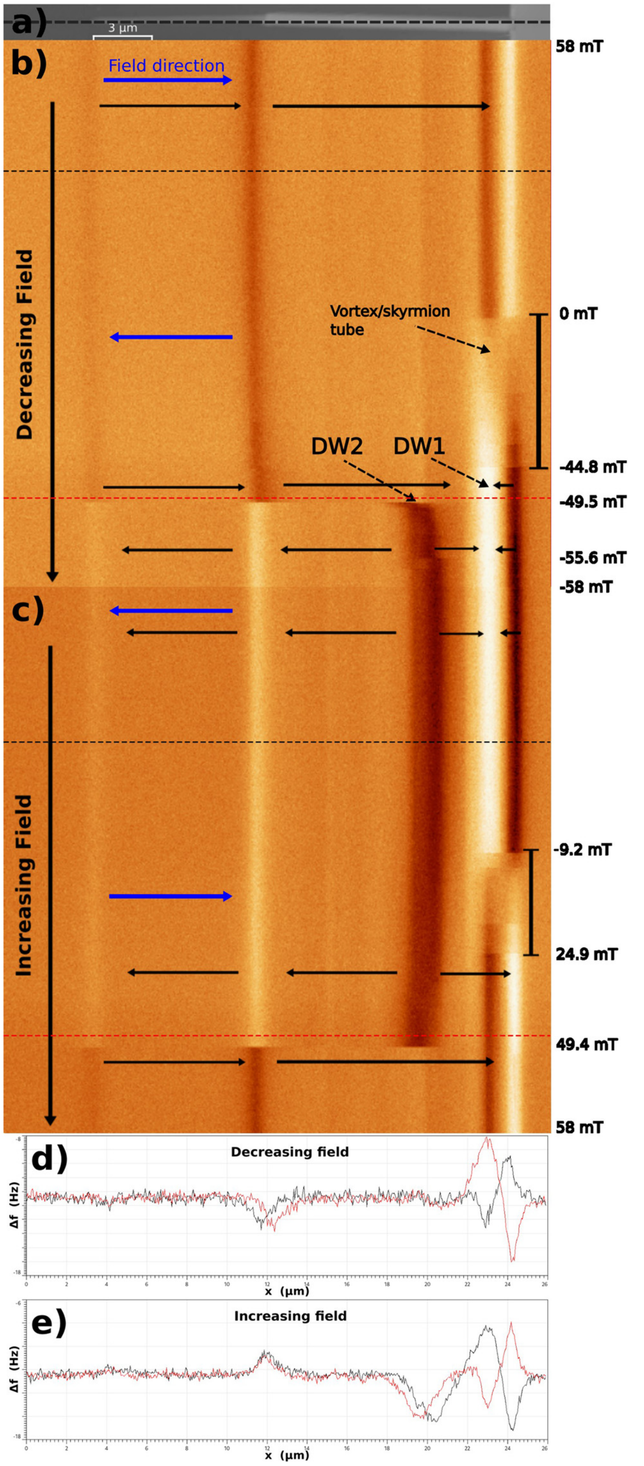

Fig. 8 3D-mode imaging of the BNW, plotted against an external field applied parallel to the NWs' long axis. (a) Standard AFM topography map. The grey dashed line represents the scanned line for the 3D-mode measurement. (b and c) 3D plots for decreasing and increasing magnetic fields, respectively. The black horizontal arrows represent the magnetisation direction. The brackets indicate the magnetic configurations for which the magnetic charges are compensated at the right end of the BNW. (d and e) Phase shift profiles taken along the black and red dashed lines in (b) and (c), respectively.

respectively), as shown in Fig. 2 and 3. A DW becomes clearly pronounced when the spot is at its darkest around −29 mT, which is characteristic of a longitudinal domain at the right side of the BNW.

As the applied field decreases (becoming more negative), the DW sequentially unpins and pins at several defects along the wide segment. Some stray field is leaked from these defects, which is detected using an MFM probe and results in the vertical lines in the 3D mode images, which match the location where the DW pins. The DW then finally unpins and propagates through the narrow segment reversing the magnetisation in a single step. As predicted by the micromagnetic simulations, there is no DW pinning induced by the sharp modulation in diameter.

Fig. 7 and 8 present another representative result of a different BNW and correspond to the standard VF-MFM and 3D operation mode, respectively. This time, the external field starts at 58 mT and again, just after remanence, the compensation of magnetic charges is observed, as a DW nucleates at −44.8 mT, evidencing a skyrmion tube-mediated DW nucleation process. We call this first DW1 as indicated in Fig. 7 and 8. However, in this NW, DW1 is pinned in such a way that the magnetisation of the narrow segment and the left part of the wide segment reverse before the DW is unpinned. This results in a second DW being nucleated, which we call DW2, and a magnetic domain in the wide segment on the left is still magnetised in the +*x* direction between two strongly pinned DWs.

Fig. 8(d) and 8(c) show the profiles of the frequency shift taken along the black and red dashed lines for the decreasing and increasing applied fields, respectively. In 8(d), it is clear that the dark spot at the diameter modulation shifts to the right before the nucleation of DW2. This is in agreement with the expansion of a vortex in the modulation into the wide segment in the simulation results. It is not entirely unreasonable to conclude that the magnetisation reversal of the left part of the BNW (left of DW2) occurs due to the creation of a pair of DWs at the diameter modulation which propagate in opposite directions, resulting in a reversed segment and DW2.

In our MFM set-up, we could not apply enough magnetic field to depin either of the two DWs. Fig. 8(b) and (c) show a minor hysteresis loop of the magnetisation. During the field increase, between −9 mT and 24.9 mT, the magnetic charge compensation is again observed, evidencing a skyrmion tube-mediated process that annihilates DW1.

Lastly, at 49.4 mT, the NW is again completely magnetised in the +*x* direction. The fact that DW2 shifts to the left side before the complete reversal while the spot at the diameter modulation remains unchanged, as evidenced in 8(c) and (e), seems to indicate that this occurs by the unpinning of DW2, which propagates left, reversing the magnetisation.

Conclusions

In conclusion, our work provides new insights into the nucleation and motion of DWs in cylindrical BNWs, demonstrating the feasibility of tuning DW nucleation through geometrical modulation in bisegmented FeCo NWs. We have experimentally confirmed by MFM imaging that the DW nucleation process takes place in the wide segment and is mediated by the formation of a skyrmion tube texture. Micromagnetic simulations show that this process is qualitatively similar in Ni-based nanowires and is defined by the cylindrical geometry. Our micromagnetic simulations further revealed that field-driven BP-DW motion is intricately dependent on the chirality of the DW. Specifically, when the DW chirality opposes the natural direction of the precessional motion of the spins, DW progression is impeded by the emission of surface spin waves and further propagation requires the injection of pairs of BPs, which results in the switching of BP-DW chirality. These findings contribute to the broader understanding of DW dynamics in cylindrical magnetic systems and open avenues for future research into chirality-dependent DW manipulation. Additionally, our experimental observations highlight the significant role of structural and magnetic defects in the behavior of DWs within cylindrical BNWs. In contrast to the smooth DW motion predicted by simulations in idealized defect-free BNWs, we observed strong DW pinning effects in actual BNWs, underscoring the need to consider defect management in practical DW-based applications.

Methods

Micromagnetic simulations

Micromagnetic simulations were performed using Mumax3 open source software,[32] which solves the Landau–Lifshitz–Gilbert (LLG) equation. We considered a cylindrical bisegmented NW with 7.04 μm in length, consisting of a 5 μm wide segment and a 2 μm narrow segment. The two segments were connected by a circle-based profile made of two equal arcs of circumference with the radius $R_t = ((R_2 - R_1)^2 + \lambda^2)/(4(R_2 - R_1))$ as described in ref. 33, where the modulation length $\lambda = 40$ nm and R_1 and R_2 are the radii of two segments.

Diameters of $d = 40$ nm and $D = 120$ nm for the narrow and wide segments were considered, respectively, and lower than those of the fabricated BNWs due to computational limitations. The ratio d/D was kept as 1/3 as fabricated. A discretization cell with a size of 2.5 nm was used. Typical values for saturation magnetisation $\mu_0 M_{\text{sat}} = 2T$ and exchange stiffness $A_{\text{ex}} =$ 15 pJ for FeCo alloys were considered. The initial states were computed by attributing random cubic anisotropy axes to a grain structure modelled using a Voronoi tessellation[34] and relaxing a saturated BNW at remanence. For dynamic simulations, a low damping constant of $\alpha = 0.02$ was used to solve the LLG equation, while for computing equilibrium states, precession was disabled.

MFM images were computed from the micromagnetic data using the Ubermag[35] framework for a horizontal plane 100 nm above the top of the sample. The MFM probe is modelled as a magnetic dipole oscillating harmonically in a magnetic field (stray field). The phase shift is given by the following expression:

$$\Delta\phi = \frac{Q\mu_0}{k}\left(\mathbf{M}_\text{t} \cdot \frac{\partial^2 \mathbf{H}_\text{s}}{\partial z^2}\right)$$

where the quality factor of the cantilever $Q = 650$ is a dimensionless quantity, the spring constant $k = 3$ N m^{-1} and $\mathbf{M}_\text{t} = (0, 0, 10^{16})$ A m^{-1} is the effective dipole moment of the tip and $\mathbf{H}_\text{s}$ is the stray field of the sample in A m^{-1}. The resulting phase map corresponds to an MFM image.

Synthesis of bisegmented FeCo nanowires

Electropolished aluminum foils (99.999% purity) were electrochemically anodized for 60 minutes under HA conditions,[15] carried out at 0–3 °C in a 0.3 M oxalic acid aqueous electrolyte, which contained 5 vol% ethanol as an antifreeze agent, by applying an anodic voltage of 140 V. Additional experimental details on the HA procedure can be found elsewhere.[24–26] Subsequently, the HA membranes were immersed in a 5 wt% phosphoric acid solution at 30 °C for 30 minutes to enlarge the pore size. A protective SiO_2 layer, with approximately 4–5 nm thickness, was deposited inside the pore channels by using the ALD technique.[23] This passivating SiO_2 layer prevented further chemical etching, thus avoiding any additional enlargement of the pore diameter. The samples were then reanodized under HA conditions (140 V, 0 °C) for 15 minutes, promoting the growth of a new alumina nanopore segment that remained unprotected by the deposited SiO_2 layer. Furthermore, the unoxidized Al substrate at the bottom of the alumina membranes was selectively dissolved in a $CuCl_2$ and HCl solution. Chemical etching of the samples in 5 wt% phosphoric acid at 30 °C caused the unprotected alumina pore segment to expand to a diameter of approximately 250 nm, while the segment protected with the SiO_2 ALD layer remained unaffected. This process created a clear and sharp diameter modulation at the interface between both the SiO_2 coated and uncoated pore segments (as depicted in Fig. 1). Finally, the nanoporous HA templates were coated with an additional SiO_2 thin layer of approximately 3.5 nm to prevent any single metallic nanowire from chemical corrosion, when releasing them from the HA alumina template.

The HA membranes described above were employed as starting templates for the synthesis of diameter-modulated FeCo BNWs, where a gold layer was first defined on the backside of the HA templates by sputtering, followed by electrodeposition of a commercial Au plating bath. The as-obtained membranes were then used as working electrodes for the pulsed electrodeposition of FeCo alloy nanowires, which were grown inside the nanopores of the template from an electrolyte containing 0.06 M $CoSO_4$, 0.13 M $FeSO_4$, and 0.16 M H_3BO_3. Continuous nitrogen (N_2) bubbling was also applied during both the electrolyte preparation and the electrodeposition process, to prevent oxidation of Fe^{2+} ions. The pulsed electrodeposition sequence involved 3000 pulses of 0.5 s at a constant voltage of −1.8 V, measured relative to an Ag/AgCl reference electrode, with resting pulses of 0.5 s at open circuit potential between each deposition pulse.

Variable-field magnetic force microscopy (VF-MFM)

MFM measurements were performed using a system from Nanotec Electrónica S.L. controlled by WSxM software[36] and commercial high magnetic moment probes from Nanosensors. The scanning was performed in amplitude-modulation mode, where the signals' amplitude was used as a feedback parameter to obtain a topographic map. The second scan was performed under a phase-lock-loop (PLL) system, which attempts to keep the phase constant so the magnetic signal is given by a frequency shift. The sample was placed between two soft iron pieces connected to an electromagnetic coil, thereby applying an external magnetic field longitudinally along the nanowire axis. 3D operation mode measurements were performed by continuously scanning the same line over the nanowire under a changing magnetic field.[37]

Author contributions

A. A., C. B., J. G., V. M. P. and O. C.-F. conceived the project. J. F. performed the micromagnetic simulations and MFM measurements with the assistance of O. C.-F. and A. A. Bisegmented magnetic nanowires were prepared by V. V., Y. A., and J. G. with the assistance of V. M. P. All authors discussed the results. The main text of the article was written by J. F., A. A., J. G., V. M. P. and O. C.-F. All authors contributed to the text of the article and approved it.

Conflicts of interest

There are no conflicts to declare.

Data availability

The original data can be obtained from the corresponding authors upon request.

Acknowledgements

The authors gratefully acknowledge the financial support from the Spanish Ministry of Innovation and Science MCIN/ AEI/ 10.13039/501100011033 under projects no PID2022-137567NB-C21, PID2022-137567NB-C22 and PID2022-138169OB-I00. Y. A. wishes to thank the regional government of the Principality of Asturias for the financial support under the Severo Ochoa grant (ref.: PA-23-BP22-144). Scientific and technical support provided by Common Research Services (SCTs) from the University of Oviedo is also gratefully acknowledged.

References

1 H. Masuda and K. Fukuda, *Science*, 1995, **268**, 1466–1468.

2 A. Li, F. Müller, A. Birner, K. Nielsch and U. Gösele, *J. Appl. Phys.*, 1998, **84**, 6023–6026.

3 K. Nielsch, F. Müller, A.-P. Li and U. Gösele, *Adv. Mater.*, 2000, **12**, 582–586.

4 A. Fernández-Pacheco, R. Streubel, O. Fruchart, R. Hertel, P. Fischer and R. P. Cowburn, *Nat. Commun.*, 2017, **8**, 1–14.

5 R. Streubel, P. Fischer, F. Kronast, V. P. Kravchuk, D. D. Sheka, Y. Gaididei, O. G. Schmidt and D. Makarov, *J. Phys. D: Appl. Phys.*, 2016, **49**, 363001.

6 C. Ferguson, D. MacLaren and S. McVitie, *J. Magn. Magn. Mater.*, 2015, **381**, 457–462.

7 C. Bran, J. A. Fernandez-Roldan, R. P. Del Real, A. Asenjo, O. Chubykalo-Fesenko and M. Vazquez, *Nanomaterials*, 2021, **11**, 600.

8 R. Hertel, *J. Phys.: Condens. Matter*, 2016, **28**, 483002.

9 A. Wartelle, B. Trapp, M. Staňo, C. Thirion, S. Bochmann, J. Bachmann, M. Foerster, L. Aballe, T. Menteş, A. Locatelli, *et al.*, *Phys. Rev. B*, 2019, **99**, 024433.

10 F. Tejo, J. A. Fernandez-Roldan, K. Y. Guslienko, R. M. Otxoa and O. Chubykalo-Fesenko, *Nanoscale*, 2024, **16**, 10737–10744.

11 M. Charilaou, H.-B. Braun and J. F. Löffler, *Phys. Rev. Lett.*, 2018, **121**, 097202.

12 J. A. Fernandez-Roldan, R. P. Del Real, C. Bran, M. Vazquez and O. Chubykalo-Fesenko, *Nanoscale*, 2018, **10**, 5923–5927.

13 E. Berganza, J. Marqués-Marchán, C. Bran, M. Vazquez, A. Asenjo and M. Jaafar, *Materials*, 2021, **14**, 5671.

14 J. Marqués-Marchán, J. A. Fernandez-Roldan, C. Bran, R. Puttock, C. Barton, J. A. Moreno, J. Kosel, M. Vazquez, O. Kazakova, O. Chubykalo-Fesenko, *et al.*, *Nanomaterials*, 2022, **12**, 1968.

15 W. Lee, R. Ji, U. Gösele and K. Nielsch, *Nat. Mater.*, 2006, **5**, 741–747.

16 Y. P. Ivanov, M. Vázquez and O. Chubykalo-Fesenko, *J. Phys. D: Appl. Phys.*, 2013, **46**, 485001.

17 C. Bran, E. Berganza, J. A. Fernandez-Roldan, E. M. Palmero, J. Meier, E. Calle, M. Jaafar, M. Foerster, L. Aballe, A. Fraile Rodriguez, *et al.*, *ACS Nano*, 2018, **12**, 5932–5939.

18 C. Bran, E. Saugar, J. A. Fernandez-Roldan, R. P. del Real, A. Asenjo, L. Aballe, M. Foerster, A. Fraile Rodríguez, E. M. Palmero, M. Vazquez and O. Chubykalo-Fesenko, *Nanoscale*, 2021, **13**, 12587–12593.

19 V. M. Prida, J. García, L. Iglesias, V. Vega, D. Görlitz, E. D. Nielsch, K. Barriga-Castro, R. Mendoza-Reséndez, A. Ponce and C. Luna, *Nanoscale Res. Lett.*, 2013, **8**, 263.

20 J. García Fernández, V. Vega Martínez, A. Thomas, V. M. De La Prida Pidal and K. Nielsch, *Nanomaterials*, 2018, **8**, 548.

21 J. A. Moreno and J. Kosel, *Sci. Rep.*, 2022, **12**, 19510.

22 J. Cantu-Valle, E. D. Barriga-Castro, V. Vega, J. García, R. Mendoza-Reséndez, C. Luna, V. M. Prida, K. Nielsch, F. Mendoza-Santoyo, M. Jose-Yacaman and A. Ponce, *J. Magn. Magn. Mater.*, 2015, **379**, 294–299.

23 J. Bachmann, R. Zierold, Y. Tung Chong, R. Hauert, C. Sturm, R. Schmidt-Grund, B. Rheinländer, M. Grundmann, U. Gösele and K. Nielsch, *Angew. Chem., Int. Ed.*, 2008, **47**, 6177–6179.

24 M. Méndez, V. Vega, S. González, R. Caballero-Flores, J. García and V. M. Prida, *Nanomaterials*, 2018, **8**, 595.
25 E. M. Palmero, M. Mendez, S. Gonzalez, C. Bran, V. Vega, M. Vazquez and V. M. Prida, *Nano Res.*, 2019, **12**, 1547–1553.
26 J. García, J. A. Fernández-Roldán, R. González, M. Méndez, C. Bran, V. Vega, S. González, M. Vázquez and V. M. Prida, *Nanomaterials*, 2021, **11**, 3077.
27 R. Hertel and J. Kirschner, *J. Magn. Magn. Mater.*, 2004, **278**, L291–L297.
28 R. Hertel and J. Kirschner, *Phys. B*, 2004, **343**, 206–210.
29 M. Yan, C. Andreas, A. Kákay, F. García-Sánchez and R. Hertel, *Appl. Phys. Lett.*, 2012, **100**, 252401.
30 J. Fernandez-Roldan and O. Chubykalo-Fesenko, *APL Mater.*, 2022, **10**, 111101.
31 U. Celano, P. Rickhaus, C. Bran, J. Marqués-Marchán, V. J. Borràs, M. Korytov, A. Asenjo and M. Vazquez, *Nanoscale*, 2024, **16**, 16838–16843.
32 A. Vansteenkiste, J. Leliaert, M. Dvornik, M. Helsen, F. Garcia-Sanchez and B. Van Waeyenberge, *AIP Adv.*, 2014, **4**, 107133.
33 J. A. Fernández-Roldán, A. De Riz, B. Trapp, C. Thirion, M. Vazquez, J.-C. Toussaint, O. Fruchart and D. Gusakova, *Sci. Rep.*, 2019, **9**, 1–12.
34 J. Leliaert, B. Van de Wiele, A. Vansteenkiste, L. Laurson, G. Durin, L. Dupré and B. Van Waeyenberge, *J. Appl. Phys.*, 2014, **115**, 233903.
35 M. Beg, M. Lang and H. Fangohr, *IEEE Trans. Magn.*, 2022, **58**, 1–5.
36 I. Horcas, R. Fernández, J. Gomez-Rodriguez, J. Colchero, J. Gómez-Herrero and A. Baro, *Rev. Sci. Instrum.*, 2007, **78**, 013705.
37 M. Jaafar, L. Serrano-Ramón, O. Iglesias-Freire, A. Fernández-Pacheco, M. R. Ibarra, J. M. De Teresa and A. Asenjo, *Nanoscale Res. Lett.*, 2011, **6**, 1–6.